INTERIM REPORT

Advanced Signal Processing for Detailed Site Characterization and Target Discrimination

SERDP Project MR-1669

APRIL 2001

Peter B. Weichman
BAE Systems

SERDP
DOD · EPA · DOE

		Form Approved OMB No. 0704-0188
Report Documentation Page		

Public reporting burden for the collection of information is estimated to average 1 hour per response, including the time for reviewing instructions, searching existing data sources, gathering and maintaining the data needed, and completing and reviewing the collection of information. Send comments regarding this burden estimate or any other aspect of this collection of information, including suggestions for reducing this burden, to Washington Headquarters Services, Directorate for Information Operations and Reports, 1215 Jefferson Davis Highway, Suite 1204, Arlington VA 22202-4302. Respondents should be aware that notwithstanding any other provision of law, no person shall be subject to a penalty for failing to comply with a collection of information if it does not display a currently valid OMB control number.

1. REPORT DATE **APR 2001**	2. REPORT TYPE **N/A**	3. DATES COVERED **-**

4. TITLE AND SUBTITLE **Advanced Signal Processing for Detailed Site Characterization and Target Discrimination**	5a. CONTRACT NUMBER
	5b. GRANT NUMBER
	5c. PROGRAM ELEMENT NUMBER
6. AUTHOR(S)	5d. PROJECT NUMBER
	5e. TASK NUMBER
	5f. WORK UNIT NUMBER
7. PERFORMING ORGANIZATION NAME(S) AND ADDRESS(ES) **BAE Systems**	8. PERFORMING ORGANIZATION REPORT NUMBER
9. SPONSORING/MONITORING AGENCY NAME(S) AND ADDRESS(ES)	10. SPONSOR/MONITOR'S ACRONYM(S)
	11. SPONSOR/MONITOR'S REPORT NUMBER(S)

12. DISTRIBUTION/AVAILABILITY STATEMENT **Approved for public release, distribution unlimited**

13. SUPPLEMENTARY NOTES **The original document contains color images.**

14. ABSTRACT

15. SUBJECT TERMS

16. SECURITY CLASSIFICATION OF:			17. LIMITATION OF ABSTRACT **SAR**	18. NUMBER OF PAGES **16**	19a. NAME OF RESPONSIBLE PERSON
a. REPORT **unclassified**	b. ABSTRACT **unclassified**	c. THIS PAGE **unclassified**			

Standard Form 298 (Rev. 8-98)
Prescribed by ANSI Std Z39-18

Advanced Signal Processing for Detailed Site Characterization and Target Discrimination (Project 1669)
Interim Report: EMI Model Validation Using NRL TEMTADS Data

Peter B. Weichman

BAE Systems, Advanced Information Technologies,
6 New England Executive Park, Burlington, MA 01803

This report details basic validation of our physics-based EMI models against data collected by the NRL TEMTADS system. The data was collected under laboratory-type conditions using artificial spheroidal targets. The models are essentially exact for these types of targets, and enable detailed comparison of theory and data in support of both model validation and measurement platform characterization.

I. INTRODUCTION

This document details successful validation of our physics-based "mean field" and "early time" approaches to modeling of time-domain electromagnetic (TDEM) responses of compact, highly conducting targets. Specifically, we apply our methods to the analysis of laboratory-style data collected by the NRL TEMTADS system using artificial spheroidal targets. The models use the detailed system parameters (transmitter and receiver coil position, orientation, and geometry; transmitted pulse waveform; target position, orientation, geometry; target conductivity and permeability) to generate first principles predictions for the measured time-domain voltages. The models are designed to be essentially exact for spheroidal targets, and, as described in the remainder of this document, the remarkable agreement between measurements and predictions strongly supports this conclusion.

The outline of the remainder of this document is as follows. Details of the EM theory underlying the models, and their numerical implementation, will be detailed elsewhere, but a basic overview is given in Sec. II. In Sec. III the basic parameters of the NRL TEMTADS system are detailed. In Sec. IV model predictions are compared with TEMTADS data for spherical targets, for which an exact analytic theory also exists (Sec. IV A); prolate (elongated) and oblate (discus-like) spheroidal targets (Sec. IV B). Finally, conclusions and directions for future work are presented in Sec. V.

II. MODELING BACKGROUND

The essence of the TDEM induction measurement is sketched in Fig. 1. The transmitter loop current pulse generates a magnetic field in the target region. This changing applied field, especially as the pulse terminates, induces currents in the target, generating a scattered magnetic field. The decaying scattered field, following pulse termination, induces the measured voltage in the receiver loop.

There are three different regimes that one may identify in the voltage time traces: early, intermediate, and late
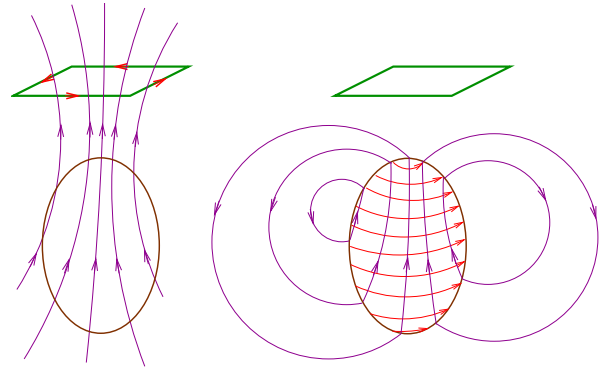

FIG. 1: Sketch of target EMI response. **Left:** The transmitter current induces a magnetic field inside the target. **Right:** The transmitter pulse termination induces screening currents in the target that, via Lens's law, oppose the change in the applied field. These currents are initially confined to the target surface, but then diffuse inward, generating a decaying scattering magnetic field that is sensed though the induced voltage in the receiver loop.

time. At very early time, immediately following pulse termination, the currents are confined to the immediate surface of the target. The initial diffusion of these currents into the target interior leads to a power law decay ($1/t^{1/2}$ for nonferrous targets, $1/t^{3/2}$ for ferrous targets [1, 2]). At intermediate time, as the currents penetrate the deeper target interior, the power law crosses over to a multi-exponential decay, representing the simultaneous presence of a finite set of exponentially decaying modes. Finally, at late time only the single, slowest decaying mode survives.

At intermediate- to late-time our mean field algorithm models the dynamics by computing as large a number as possible of the modes, and determining the excitation level of each. At early time, the power law arises from a superposition of an essentially infinite number of exponentials, and a complementary theory, based on the detailed dynamics of the initial very thin surface current sheet, has been developed instead.

A. intermediate- to late-time modeling: mean field approach

The solution to the Maxwell equations allows one to represent the electric field following pulse termination as a sum of exponentially decaying modes,

$$\mathbf{E}(\mathbf{x}, t) = \sum_{n=1}^{\infty} A_n \mathbf{e}^{(n)}(\mathbf{x}) e^{-\lambda_n t} \tag{2.1}$$

where λ_n are decay rates, $\mathbf{e}^{(n)}$ are mode shapes, and A_n are excitation coefficients. The first two are intrinsic properties of the target, analogous to vibration modes of a drumhead. Only the excitation amplitudes actually depend on the measurement protocol.

As time progresses, modes with larger values of λ_n decay more quickly, and so at any given time t the signal will be dominated by some finite set of modes, namely those modes with $\lambda_n \lesssim 1/t$. At very late time, $t > 1/\lambda_1$, only the slowest decaying mode contributes, and the signal becomes a pure exponential decay. Thus, the earlier in time one wishes to model quantitatively, the greater the number of modes that are required. The ultimate limitation turns out to be the rate at which the excitation in pulse is terminated. If the pulse is turned off on a time scale t_r (see Sec. III B), then only modes with $\lambda_n \lesssim 1/t_r$ have substantial amplitudes A_n, and a finite set of modes suffices for a full description of the target electrodynamics. However, for large targets, this may require many thousands, or even tens of thousands, of modes, which is beyond current computational capability. However, the early time power law regime may extend out to 1 ms, or even 10's of ms, and we will see that a few hundred modes is more than enough to overlap this regime. The early time (see Sec. II B) and mean field approaches may then be combined to fully describe the target dynamics over the full measured time range.

Using the mode orthogonality relation,

$$\int d^3 x \sigma(\mathbf{x}) \mathbf{e}^{(m)*}(\mathbf{x}) \cdot \mathbf{e}^{(n)}(\mathbf{x}) = \delta_{mn}, \tag{2.2}$$

where $\sigma(\mathbf{x})$ is the conductivity, the excitation amplitude can be shown to be given by

$$A_n = I_T^{(n)} N_T \int_{C_T} \mathbf{e}^{(n)*}(\mathbf{x}) \cdot d\mathbf{l}, \tag{2.3}$$

in which the transmitter loop has been approximated by an ideal 1D loop C_T with N_T windings, and

$$I_T^{(n)} = - \int_{-\infty}^{0} dt e^{\lambda_n t} \partial_t I_T(t) \tag{2.4}$$

depends on the history transmitter loop current $I_T(t)$ up until the beginning of the measurement window, taken here as $t = 0$. To gain some intuition, a single perfect square wave pulse of amplitude I_T^0 and duration t_p, one obtains

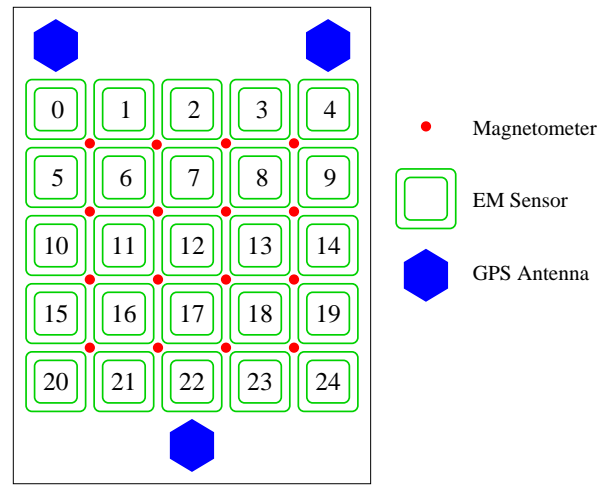$$I_T^{(n)} = I_T^0 (1 - e^{-\lambda_n t_p}). \tag{2.5}$$

FIG. 2: Sketch of NRL TEMTADS array consisting of a 5×5 array of 25 independent, concentric transmitter and receiver coils, numbered from 0 to 24 as shown. Due to rapid decay of signals with target depth, precise (cm level) geometry and placement of the coils (summarized in Table I) can have significant effect on the overall measured voltage amplitude.

Sensor center horizontal separation	40 cm
Transmitter coil center height	4.3 cm
Transmitter diameter	35 cm
Number of transmitter coil windings N_T	35
Receiver coil center height	0.4 cm
Receiver diameter	25 cm
Number of receiver coil windings N_R	16

TABLE I: NRL TEMTADS array geometry. The transmitter coil windings are 7.8 cm tall with 0.4 cm thick endcaps on top and bottom. Height is measured from the bottom side of the lower endcap, and the transmitters are then modeled as an idealized 1D square loops at $0.4 + 3.9 = 4.3$ cm height. The receiver coils are vertically compact and lie at the bases of the transmitter coils, hence are modeled as idealized 1D square loops at 0.4 cm height.

For a mode that decays rapidly on the scale t_p, one has $\lambda_n t_p \gg 1$, and $I_T^{(n)} \simeq I_T^0$. For a more slowly decaying modes, $I_T^{(n)}$ will have a strong dependence on t_p and n. In fact, for large targets one may actually encounter the regime $\lambda_n t_p \ll 1$ [e.g., $t_p = 25$ ms and $\tau_n = 1/\lambda_n = O(100$ ms$)$] where $I_T^{(n)}$ will depend not only on t_p, but on previous pulses.

Finally, the measured voltage takes the form

$$V(t) = \sum_{n=1}^{\infty} V_n e^{-\lambda_n t} \tag{2.6}$$

in which, approximating the receiver as well by an ideal 1D loop C_R with N_R windings, the voltage amplitudes are given by the line integrals

$$V_n = A_n N_R \int_{C_R} \mathbf{e}^{(n)}(\mathbf{x}) \cdot d\mathbf{l}. \tag{2.7}$$
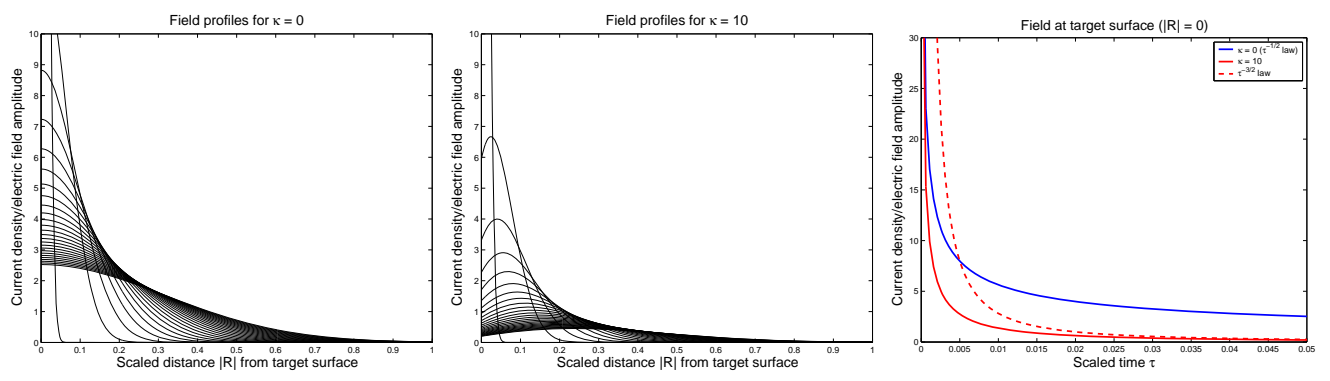
FIG. 3: Illustration of the early time evolution of the surface density depth profile from the target surface for nonmagnetic (left) and magnetic (center) targets, beginning from a delta-function initial condition (perfect step function pulse termination). Distance $R = r/L$ is scaled by the target size, time $\tau = t/\tau_D$ by the diffusion time, so that κ here corresponds $\kappa_n \sqrt{\tau_c}$ in (2.11), and is essentially the permeability contrast $(\mu - \mu_b)/\mu_b$. The profiles are plotted for a sequence of 26 equally spaced scaled times $10^{-4} \leq \tau \leq 0.05$ (earlier times corresponding to narrower profiles). The nonmagnetic profile exhibits a pure Gaussian spreading into the target interior, while the magnetic profile is much more complex due to the surface magnetic boundary condition. Its maximum is pushed inwards from the boundary, and decays more rapidly with time. The right plot shows the time trace for the current density at the surface, $R = 0$, and is essentially the profile $H(\kappa\sqrt{\tau})$, equation (2.12), which appears in the measured voltage (2.11). For $\kappa = 0$ (solid blue line) the τ-dependence follows an exact $1/\sqrt{\tau}$ power law. For $\kappa > 0$ (solid red line) the τ-dependence crosses over from the identical $1/\sqrt{\tau}$ form at early-early time to the $1/\tau^{3/2}$ power law (dashed red line) at late-early time [the asymptotic forms displayed in (2.12)].

Equations (2.3)–(2.7) provide all the required ingredients for generating predicted data based on a target and measurement platform model. Our "mean field" numerical code divides naturally into two parts.

The *internal code* solves the Maxwell equations to produce the intrinsic mode quantities λ_n and $\mathbf{e}^{(n)}$ for a range of expected targets. With increasing λ_n, the modes have more complex spatial structure, and finite numerical precision means that only a finite set (a few hundred) of slowest decaying modes are actually produced.

The *external* code uses the mode data, along with the measurement platform data, to compute current integrals (2.4), the line integrals in (2.3) and (2.7), and then combines them to output the voltage amplitudes V_n and hence the time series (2.6). Note that the line integral computation requires full knowledge of the relative position and orientation of the target and platform.

For high precision, the internal code can take anywhere from minutes to hours to produce mode data for a single target. However, given this data, the external code takes at most a few seconds produce the full predictions. Precomputation and storage of a rapidly accessible database of target data is therefore essential.

B. Complementary early time modeling

For a rapidly terminated transmitter pulse, the external electric field, and induced voltage, display an early time power law divergence [1, 2] (saturating at very early time only on the scale of the off-ramp time t_r [4]). The boundary between the intermediate (multi-exponential) and late time (mono-exponential) regime occurs at the

diffusion time scale

$$\tau_D = L^2/D \qquad (2.8)$$

where L is the characteristic target radius, and $D = c^2/4\pi\mu\sigma$ is the EM diffusion constant—this is the time scale required for the initial surface currents to diffuse into the center of the target. The early time regime corresponds to times $t \ll \tau_D$ (say, $t < \tau_D/100$), beginning deep into the multi-exponential regime where many (e.g., hundreds of) modes are excited. In this regime, for non-permeable, or weakly permeable targets ($\mu \simeq \mu_b$), one obtains the simple power law prediction prediction [1]

$$V(t) = V_e/t^{1/2}, \ t \ll \tau_D, \qquad (2.9)$$

with all of the target and measurement parameters encompassed by the single amplitude V_e, whose computation requires the solution of a certain Neumann problem for the Laplace equation in the space external to the target.

For permeable targets, a new magnetic time scale

$$\tau_{\mathrm{mag}} = \tau_D(\mu_b/\mu)^2 \qquad (2.10)$$

emerges. For ferrous targets, $\mu/\mu_b = O(100)$, and $\tau_{\mathrm{mag}}/\tau_c = O(10^{-4})$ is tiny, and the early time voltage has a more complex *magnetic surface mode* structure,

$$V(t) = \sum_{n=1}^{\infty} V_n^e H(\kappa_n\sqrt{t}) \qquad (2.11)$$

where the κ_n are surface mode eigenvalues, and the mode

eigenvector 1

eigenvector 2

eigenvector 3

eigenvectors 4,5

eigenvectors 6,7

eigenvector 8

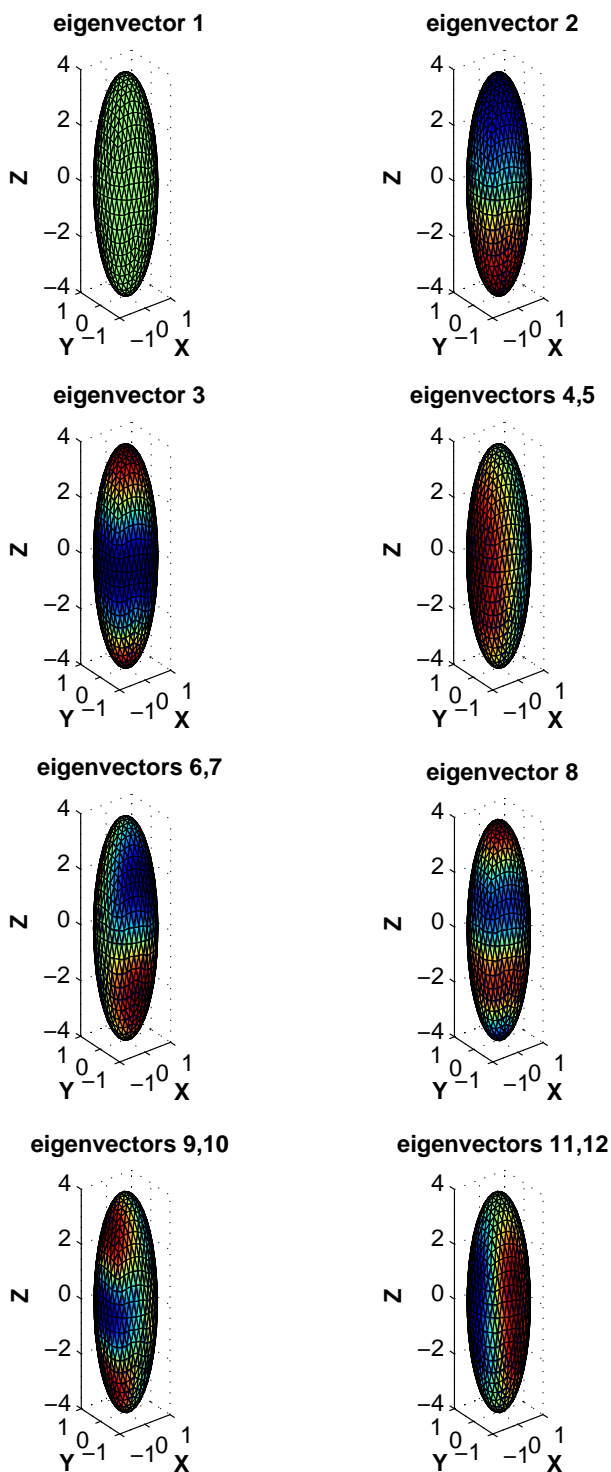**eigenvectors 9,10**

eigenvectors 11,12

FIG. 4: Contour plots for the first few magnetic surface modes eigenfunctions for an aspect ratio 4 prolate spheroid. Plotted is the *stream function* ψ_n associated with each mode: red corresponds to positive ψ_n, blue to negative ψ_n, and green to near zero values (node lines). The level curves of ψ_n are the stream lines of the surface current. Higher order eigenfunctions clearly have more complex structure with patterns of multiple, oppositely oriented current vortices (which circulate clockwise around blue patches, and counter clockwise around red patches).

time trace profile

$$
\begin{aligned}
H(s) &= \frac{1}{\sqrt{\pi}s} - e^{s^2}\mathrm{erfc}(s) \\
&\approx \begin{cases} \frac{1}{\sqrt{\pi}s}, & s \ll 1 \\ \frac{1}{2\sqrt{\pi}s^3}, & s \gg 1, \end{cases}
\end{aligned}
\tag{2.12}
$$

where $\mathrm{erfc}(s)$ is the complementary error function, interpolates between a $1/t^{1/2}$ power law at early-early time, $t \ll \tau_{\mathrm{mag}}$, and a $1/t^{3/2}$ power law at late-early time, $\tau_{\mathrm{mag}} \ll t \ll \tau_D$. For large ferrous targets, this latter interval is very large, and may, in fact, accurately represent the signal over nearly the entire measurement interval (see Sec. IV).

Figure 3 illustrates the important features of the early time modeling, including the complex evolution of the surface current depth profile [which extends $H(s)$ to a function of both time and space [2]] that ultimately gives rise to the externally measured voltage (2.11).

The surface modes are special surface current profiles (see Fig. 4) that, instead of decaying exponentially, evolve according to the universal function $H(s)$. They and the κ_n are solutions to an eigenvalue problem defined on the surface of the target [2]. They may be determined analytically only for spherical targets, where one finds

$$
\kappa_l = l/\sqrt{\tau_{\mathrm{mag}}}, \ l = 1, 2, 3, \ldots,
\tag{2.13}
$$

each $(2l + 1)$-degenerate, with $\tau_{\mathrm{mag}} = 4\pi\sigma\mu_b^2 a^2/\mu c^2$, where a is the radius. The amplitudes V_n^e again require a solution to an external Laplace-Neumann problem.

Unlike the bulk, exponential modes, under most conditions, only a very few surface modes are excited. The initial surface current pattern more-or-less follows the shape of the magnetic field generated by the transmitter coil. Unless the target is close to the coil, this field is fairly uniform, and the corresponding surface current density is fairly uniform as well, and can then be represented by the first few (two or three) modes. There is a very heavy numerical overhead in computing these modes and their excitation amplitudes, all in pursuit of predicting the rather limited information content of just a few coefficients. Given the success of extending the mean field predictions into the intermediate-early time regime, we have therefore found that it is much more efficient to extend the voltage curve by *fitting* the data at intermediate times to a one or two term series of the form (2.11), estimating $\kappa_n \approx 1/\sqrt{\tau_{\mathrm{mag}}}$ for the first few modes. Although this precludes quantitative predictions at early-early time, it provides an enormously useful *qualitative* confirmation that the functional form $H(s)$ accurately describes the data.
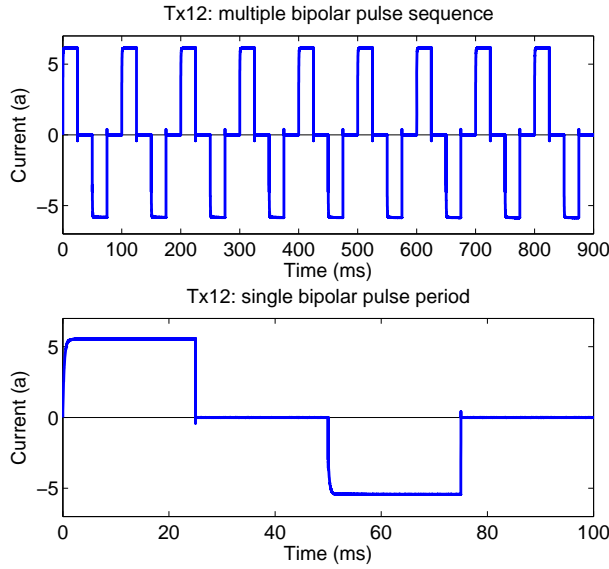
FIG. 5: TEMTADS transmitter current bipolar pulse waveform. **Top:** multiple periods. **Bottom:** single 100 ms period.

III.   TEMTADS PLATFORM

A.   Platform geometry

The 5×5 NRL TEMTADS sensor array is sketched in Fig. 2, and its geometrical parameters are summarized in Table I. The loops C_T and C_R are all modeled as perfect squares with 35 cm and 25 cm edges, respectively.

The origin is taken to be at the base of the lower endcap for sensor 12, the positive x-axis towards sensor 13, the positive y-axis towards sensor 7, and the positive z-axis vertically upwards. The transmitter and receiver loop centers then all have x- and y-coordinates that are multiples of 40 cm. The transmitters are all at $z = 4.3$ cm, and receivers are all at $z = 0.4$ cm. Target positions and orientations quoted in later sections are all in this frame of reference [3].

The precise overall voltage amplitudes, required at least for initial verification of the instrument calibration, turn out to be surprisingly sensitive to small changes in these numbers. The scattered fields may be thought of as approximately dipolar, and the voltage therefore decreases roughly as $1/d^6$ with depth d. For example, therefore, a 1 cm error for a 30 cm deep target then leads to a 20% error in the voltage amplitude. A consistent systematic error of this magnitude, in fact, is what led us to uncovering the existence of the endcaps, and the vertical offset between the transmitter and receiver loops!

B.   Transmitter waveform

The TEMTADS pulse sequence is shown in Fig. 5, and its parameters are summarized in Table II. The sequence is bipolar, meaning that the pulses alternate in sign. Each pulse is 25 ms long, followed by a 25 ms measurement window ("50% duty cycle"). Although square-wave-like, the pulses have a much more rapid termination time $t_r = 10\ \mu$s than onset time (a few ms)—see Fig. 6. It is important to understand which details of the waveform actually impact on the measurement prediction.

More quantitatively, ignoring various small spike-like features, the pulse waveform is described by the following sequence of functional forms (dashed lines in Fig. 6):

$$I(t) = \begin{cases} I_1(1 - e^{-t/\tau_1}), & 0 < t \leq t_1 \\ I(t_1) + I_2[(1-\alpha)(1 - e^{(t-t_1)/\tau_2}) + \alpha(1 - e^{-(t-t_1)/\tau_3})], & t_1 < t \leq t_p \\ I_{\max}[1 - (t - t_2)/t_r], & t_2 < t \leq t_p + t_r \\ 0, & t_p + t_r < t \leq 2t_p, \end{cases} \tag{3.1}$$

with individual pulse length $t_p = 25$ ms; very rapid exponential time constant $\tau_1 = 2.5\ \mu$s over the interval $0 < t \leq t_1 = 10\ \mu$s; superposition of much slower exponential time constants $\tau_2 = 0.33$ ms, $\tau_3 = 4$ ms over the interval $t_1 < t \leq t_p$; and linear off-ramp time $t_r = 10\ \mu$s. The second half of the full bipolar pulse, beginning at $t = 2t_p$, is the same as the one above, but inverted. The current amplitudes are $I_1 \simeq I(t_1) \simeq 2.3$ a, $I_2 \simeq 3.7$ a, and $I_{\max} = I(t_p) \simeq I_1 + I_2 \simeq 6$ a. The mixing coefficient $\alpha = 0.01$–0.02 is small, and varies substantially from pulse to pulse. However, it dominates the last 1–2% of the relaxation after the first couple of ms (see upper

and lower left panels in Fig. 6).

The functional forms in (3.1) are simple enough that analytic forms for the current coefficients (2.4) may be computed straightforwardly (though somewhat tediously). If one were interested in quantitatively describing the target dynamics through the entire pulse interval, as well as the measurement interval, all of this detail would indeed be important. However, as we will now show, the separation of time scales $t_1 \ll \tau_2 \ll \tau_3 \ll t_p$ allows one (purely for convenience) to ignore most of these details without affecting the model fidelity in the measurement interval—it is really only the current amplitude
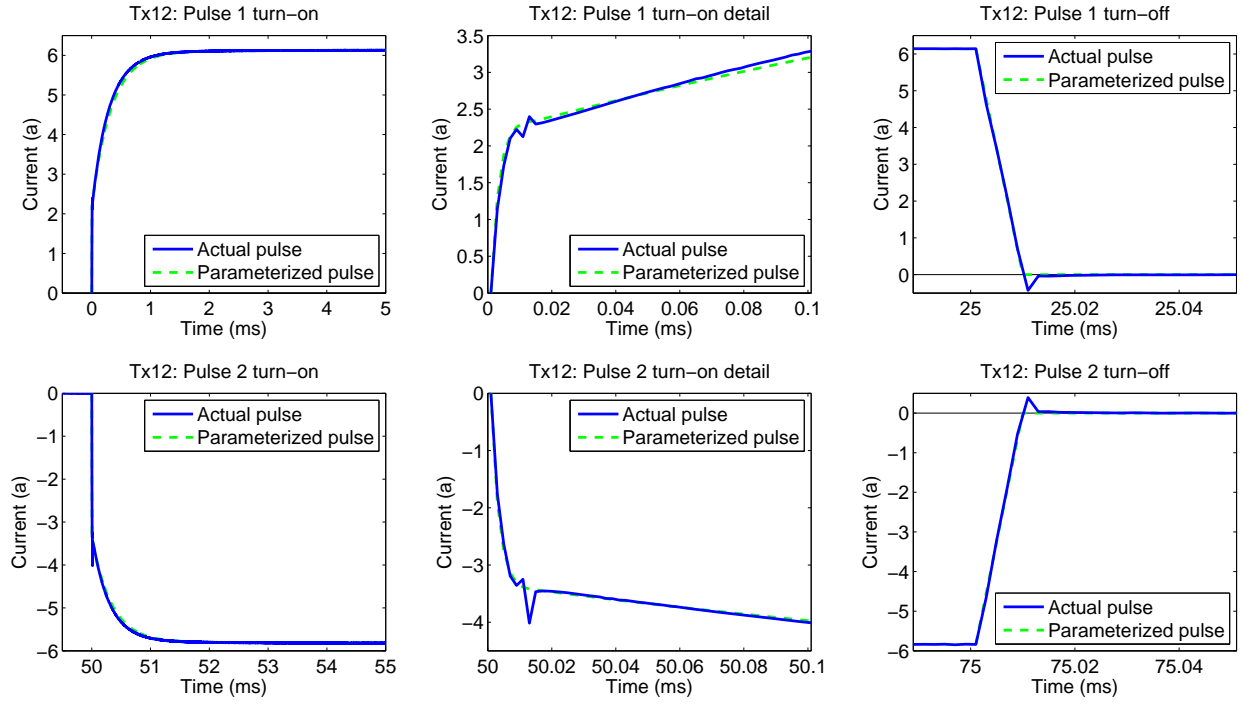
FIG. 6: Pulse waveform details, together with model fits, as described in the text, over various time intervals. The upper three plots show the positive pulse, and the lower three plots show the following negative pulse. As detailed in the text, different aspects of the shape of the pulse impact the measured (and predicted) response to differing degrees.

Transmitter current amplitude	$I_{\max} = 5.7 \pm 0.3$ a	
Full, bipolar pulse period	$T_p = 100$ ms	
Individual pulse lengths	$t_p = 25$ ms	(50% "duty cycle")
Exponential onset time constants	$\tau_1 = 2.5$ μs,	$0 \leq t < t_1 = 10$ μs
	$\tau_2 = 0.33$ ms, $\tau_3 = 4$ ms,	$t_1 \leq t < t_p$
Pulse termination linear off-ramp width	$t_r = 10$ μs	$t_p \leq t < t_p + t_r$

TABLE II: NRL TEMTADS pulse waveform parameters associated with the time traces in Fig. 6). The transmitter current amplitude varies by about 10% between pulse sequences. The pulse onset is quite complex, turning on rapidly from zero to 2.5 a over a 10 μs interval (with functional form given by an exponential with a 2.5 μs time constant), followed by a superposition of exponentials with 0.33 and 4 ms time constants, saturating at about 6 a. The pulse terminates with a 10 μs linear ramp. See equation (3.1) for precise analytic forms. Although not essential, for simplicity, the numerical model keeps only the 0.33 ms exponential onset, and the linear off-ramp.

$I_{\max}$, the pulse length t_p, and the off-ramp time t_r that matter.

To see this, note that for modes that decay rapidly enough that $\lambda_n \tau_3 \gg 1$, the $e^{\lambda_n t}$ factor makes the integral (2.4) insensitive to times prior to the pulse offset for which $I_T(t)$ differs measurably from $I_{\max}$ (i.e., times Δt such that $\Delta t / \tau_3 \ll 1$ as well). In this case $I_T^{(n)}/I_{\max}$ can depend only on the details of the off-ramp. If, in addition, $\lambda_n t_r \ll 1$ (which will be true for all modes computable using the mean field code unless the target is very small, perhaps a fraction of a cm or less in diameter), one will have $I_T^{(n)}/I_{\max} \simeq 1$.

On the other hand, for modes that decay slowly enough that $\lambda_n \tau_2 \ll 1$, the portion of the integral (2.4) arising from the pulse onset will be insensitive to the details of

this onset. The factor $e^{\lambda_n t} \simeq e^{-\lambda_n t_p}$ will be essentially constant over a time interval Δt which is up to several times τ_2 in length. One may then approximate the integral over this interval by $e^{-\lambda_n t_p} I(-t_p + \Delta t)$. Using (3.1), $I(-t_p + \Delta t)$ may be expressed entirely in terms of the τ_3 decay quantities, and may simply be approximated as $I_{\max}$ if one neglects α as well. Note that if, in addition, $\lambda t_p \ll 1$, then $I_T^{(n)}$ will be sensitive to multiple pulses. This condition is satisfied for the slowest decaying modes for large enough targets (e.g., 10 cm or more diameter steel targets).

Since the two inequalities have an overlapping range, $1/\tau_3 \ll \lambda_n \ll 1/\tau_2$, this confirms the claimed insensitivity to the onset details for all modes. In light of this, our model neglects the small parameter α, and keeps only the
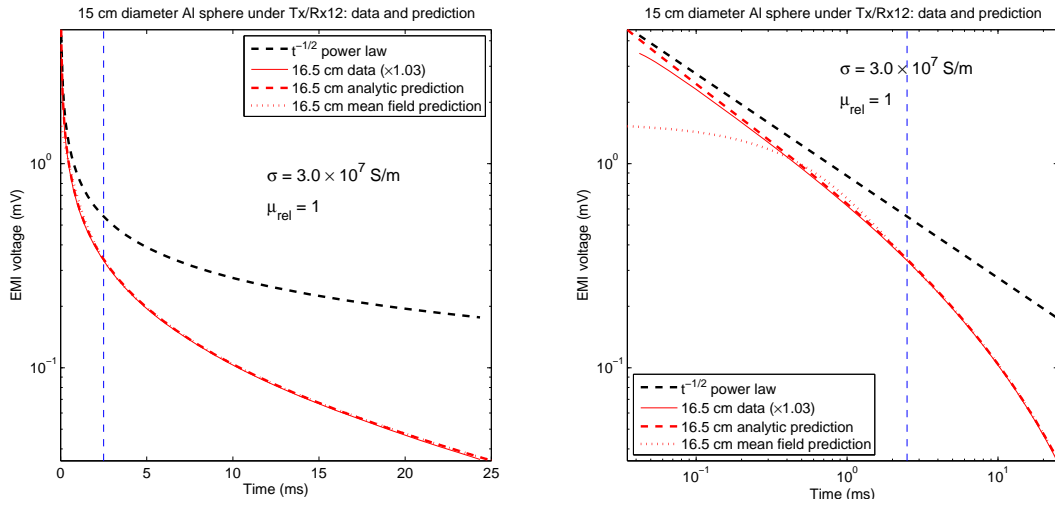
FIG. 7: Data and theory for a 15 cm diameter aluminum sphere with center lying 16.5 cm below the center of sensor 12 (see Fig. 2), which is also the only active sensor. The two plots differ only in the log vs. linear time scale. The solid red line is the data, the dashed red line the prediction from the exact analytic solution for the sphere, the dotted red line is the mean field prediction (based on 232 modes), and the dashed black line is the early time $1/\sqrt{t}$ power law. The 1.03 overall multiplier listed in the legend has been applied to the data to optimize the fit, and is well within the expected 10% fluctuation in the current amplitude. The vertical dashed line marks the rough division between the early time and multi-exponential ($\lesssim 100$ modes) regimes, and it is seen that the mean field prediction pushes well into the early time regime. The slight deviation of the data from the analytic prediction at very early time, $t < 0.1$ ms, is likely an instrument saturation effect (seen much more clearly in Fig. 8, beginning roughly at the same voltage level).
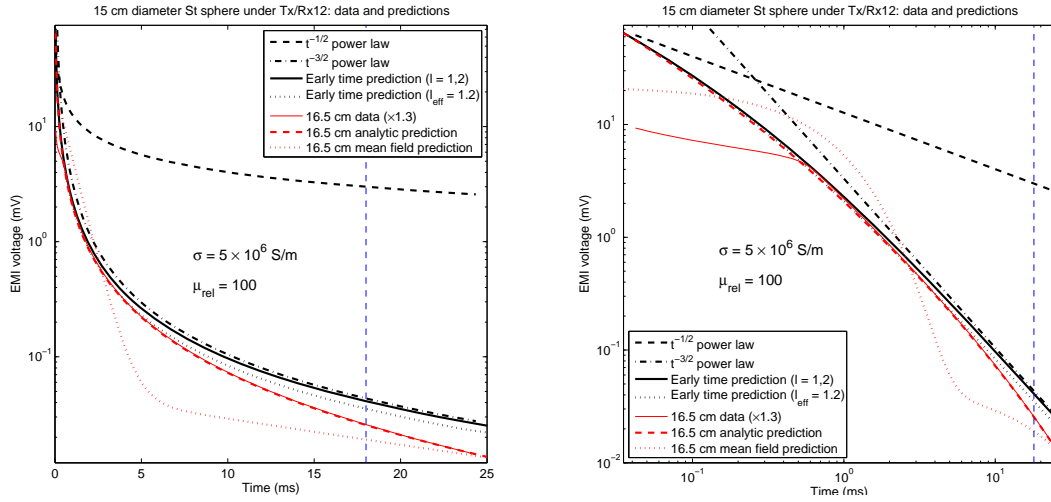

FIG. 8: Data and theory for a 15 cm diameter steel sphere with center lying 16.5 cm below the center of sensor 12 (see Fig. 2), which is also the only active sensor. The two plots differ only in the log vs. linear time scale. The solid red line is the data, the dashed red line the prediction from the exact analytic theory solution for the sphere, the dotted red line is the mean field prediction (based on 232 modes). The dashed black line is a two term fit to the early time form (2.11) using the known values (2.13), and the dotted black line is a single term fit using κ_1 as a fit parameter. The vertical dashed line marks the rough division between the early time and multi-exponential ($\lesssim 100$ modes) regimes, and is much later here than in Fig. 7 because the EM time scale is proportional to the product $\sigma\mu$, which is an order of magnitude larger here. For reasons described in the text, the mean field prediction has a more complex structure for ferrous targets, and penetrates only to the edge of the early time regime (it is the fact that it is accurate beyond about 20 ms that is the real figure of merit here, as would be more evident if the data extended to later time). The 1.3 multiplier listed in the legend is that applied to the data to optimize the fit, and lies outside the expected 10% fluctuation in the current amplitude. The difference is likely the result of small positioning errors. Sensor saturation is apparent below about 0.5 ms. The late-early time $1/t^{3/2}$ power law is evident in the data, but full convergence to the $1/\sqrt{t}$ early-early time power law is incomplete, and not expected until about 10 μs.

τ_2 decay, leading to the much simpler pulse waveform

$$I(t) = I_{\max}(1 - e^{-t/\tau_2}), \ 0 < t \le t_p, \qquad (3.2)$$

plus the identical linear off-ramp for $t_p < t \le t_p + t_r$. As shown, the separation of time scales built into the pulse waveform ensures that this simplification produces only negligible errors in the data predictions.

IV.   DATA COMPARISONS

A.   Spherical targets

Having described the electromagnetic model, and the platform model required to implement it, we now turn to its validation with real data. We will begin with spherical targets, for which exact analytic solutions exist in both the early time [1, 2] and multi-exponential regimes [5]. This allows one to validate the sensor model under conditions where the target model is fully specified.

Figure 7 shows results for a 15 cm diameter aluminum sphere, plotted on both linear and log time scales—the latter much more clearly verifies the asymptotic $1/\sqrt{t}$ early time power law. The agreement is quite remarkable—note that the vertical scale is in millivolts, not some arbitrary scaled unit. The only real fitting parameter is the conductivity, and the chosen value $\sigma = 3 \times 10^7$ S/m is well within the range expected for aluminum. As discussed in Sec. III, the overall pulse-to-pulse transmitter current amplitude is stable only at the 10% level. This leads to an identical uncertainty in the overall voltage amplitude. In the figure, an overall factor of 1.03 has been applied to the data to obtain an optimal fit, well within this uncertainty. The slowest decaying mode for this target is $\tau_1 = 21.5$ ms, so the measurement window here barely enters the late time regime $t \gtrsim \tau_1$. The mean field prediction, based on an approximate calculation of the first 232 modes, is seen to accurately describe the data well into the early time regime.

Figure 8 shows results for a 15 cm diameter steel sphere, again plotted on both linear and log time scales. The only real fitting parameters are the conductivity and relative permeability, and the chosen values $\sigma = 5 \times 10^6$ S/m and $\mu = 100$ are well within the ranges expected for steel. The overall 1.3 multiplier applied to the data lies well outside that expected based on current amplitude fluctuations alone. Fine tuning of σ and μ might account for some of this error, but, as alluded to in Sec. III A, the likely culprit is small (0.5 cm level) target positioning errors.

The mean field prediction has much more interesting structure for ferrous targets. Due to the nature of the EM boundary conditions in the large permeability contrast limit, rather than computing only the slowest decaying modes, two distinct sets of slow (169 modes in this case, with time constants larger than 3.01 ms) and fast (63 modes in this case, with time constants smaller than 0.74 ms) decaying modes are produced, with large gap between that would only be filled if one pushed the computation to higher order. This is the source of the S-curve-like structure seen in the right panel of Fig. 8. The reduction in the number of slowly decaying modes reduces the accuracy of the theory near the early–intermediate time boundary (as compared to the nonmagnetic case shown in Fig. 7), but the presence of the more rapidly decaying modes at least provides an improved trend at very early time. The slowest decaying mode for this target has a time constant $\tau_1 = 180$ ms, indicating a late time regime an order of magnitude beyond the measurement.

The early time prediction, which follows both the exact solution and the data over a significant fraction of the time interval, deserves some comment. As described in Sec. II B, to obtain the solid black lines in Fig. 7) we use the known eigenvalues (2.13), but determine the amplitudes V_n^e in (2.11) by fitting to the data. We keep only two terms

$$V(t) = V_0 \left[(1 - \alpha) H \left(\sqrt{t/t_{\mathrm{mag}}} \right) + \alpha H \left(2\sqrt{t/t_{\mathrm{mag}}} \right) \right]$$
$$(4.1)$$

with the known value $t_{\mathrm{mag}} = 0.35$ ms, and fit the amplitude $V_0 = 83$ V, and mixing parameter $\alpha = 0.4$. The one term series $V_0 = 60$ V, $\alpha = 0$ provides an adequate, but worse fit.

However, a better fit than both of these is provided by a single term series in which one allows the eigenvalue κ_1 to be adjusted. The dotted black lines in Fig. 7) shows the result obtained using $\kappa_1 = l_{\mathrm{eff}}/\sqrt{t_{\mathrm{mag}}}$ with $l_{\mathrm{eff}} = 1.2$, along with amplitude $V_1^e = 80$ V. This will be our fitting method of choice for non-spherical targets, where the eigenvalues κ_n have not yet been computed.

It is worth emphasizing the importance of the fact that analytic functional forms of the type (4.1) fit the data so well. The log-time plot demonstrates that the data span the full range over which the argument s in (2.12) interpolates between the two power laws [6]. The data therefore has significant structure through this time range, but this does not reflect any deep structure of the target (beyond the fact that it is ferrous). Quite the contrary: as illustrated in Fig. 3 it represents the dynamics of a laterally very smooth surface current sheet as it begins to penetrate the first centimeter or so into target. The complexity arises strictly from the interplay between the electric and magnetic field boundary conditions at the surface. This serves to confirm that the early time regime provides limited target discrimination ability (again, beyond the fact that it is ferrous).

Figures 9 and 10 show consolidated plots of data and theory for 10 cm and 15 cm diameter spheres at various depths centered below sensor 12. Agreement continues to be excellent. The instrument noise floor is evident for deeper targets. Further discussion may be found in the captions. All of the data curves display a tendency to flatten out at very early time, $t \lesssim 0.1$ ms, even for curves well below the obvious saturation regime. There is likely some more subtle instrument effect at work here.
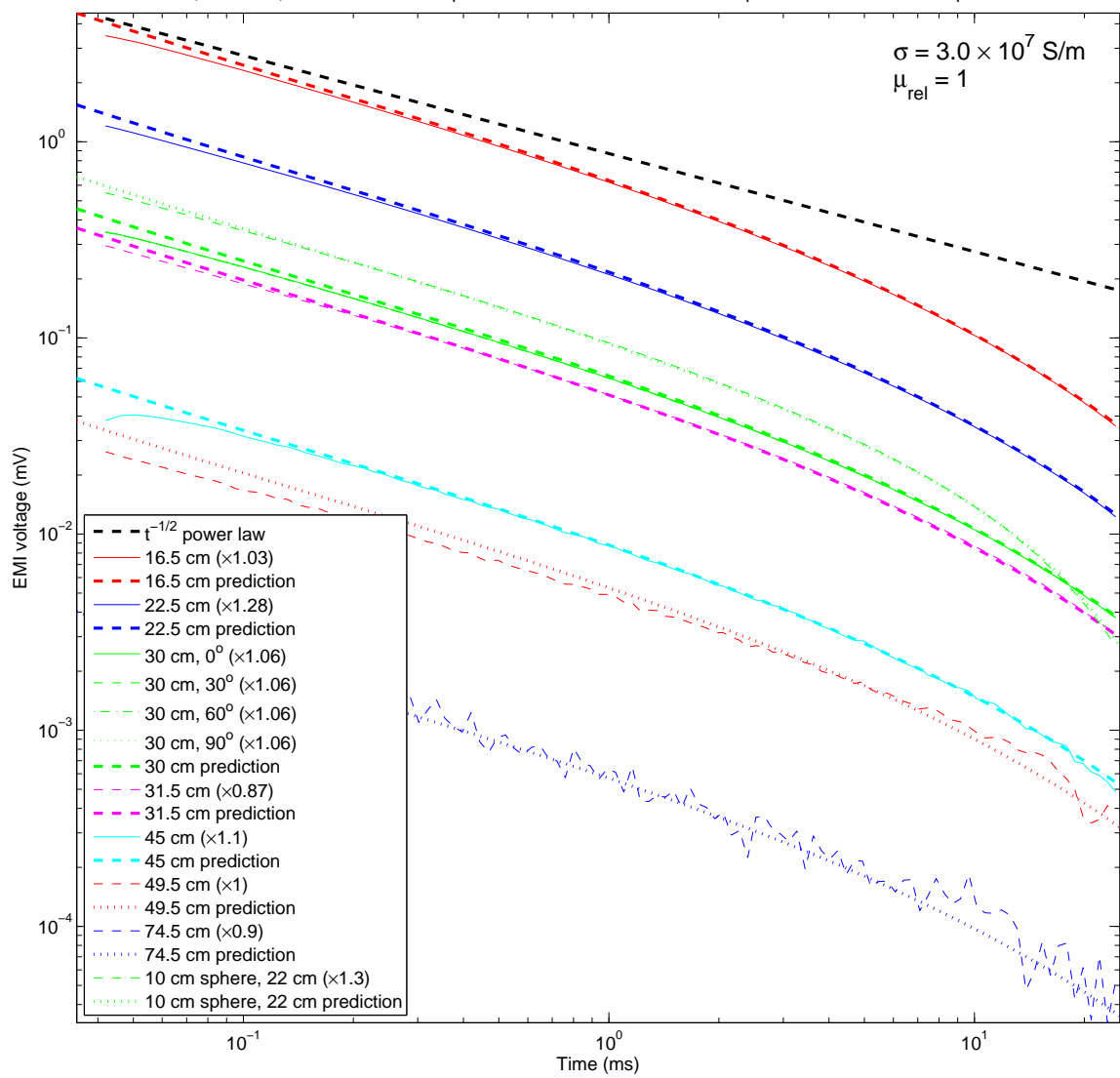
FIG. 9: Consolidated plots showing data (thin solid and dashed lines) and theory (thick dashed lines) for 10 cm and 15 cm diameter aluminum spheres at various depths centered below sensor 12. The upper curves (16.5 cm depth) are repeated from Fig. 7. The legend shows the multipliers used to scale the data curves for optimal fit. In most cases these lie within the 10% error expected from the variability of the transmitter current. Larger deviations are again likely due to small positioning errors. The four 30 cm depth curves demonstrate the expected invariance of the signal with sphere orientation ("north pole" of the sphere tilted by the indicated angles towards the center of sensor 11). The single pair of 10 cm sphere traces demonstrate the impact of target size on the late-time regime, displaying a distinctly earlier downturn.

B. Prolate and oblate spheroidal targets

Having verified instrument calibration and several other quantitative details under conditions where an exact solution exists, we now move on to spheroidal targets.

Figure 11 shows a consolidated plot of data and theory for various prolate (elongated) spheroidal aluminum targets at various depths and orientations. Spheroid aspect ratios a_z/a_{xy} vary between 2 and 5.

The theoretical plots (thick dashed lines) are the mean field predictions based on the first 232 modes. It is evident from the plots that this large a number of modes en-ables one to push the mean field predictions well into the early time regime. For smaller targets (e.g., the $4 \times 4 \times 20$ cm and $5 \times 5 \times 20$ cm spheroids) this can cover nearly the entire measurement window. The multi-exponential time series eventually saturates and falls below the data, but not before the $1/\sqrt{t}$ power law begins to be established. Interpolating between the mean field prediction and this power law clearly enables one to accurately match the data over the full range.

Most of the target discrimination information occurs at intermediate to late time. The traces are all more-or-less parallel at early time, and variations in the overall ampli-
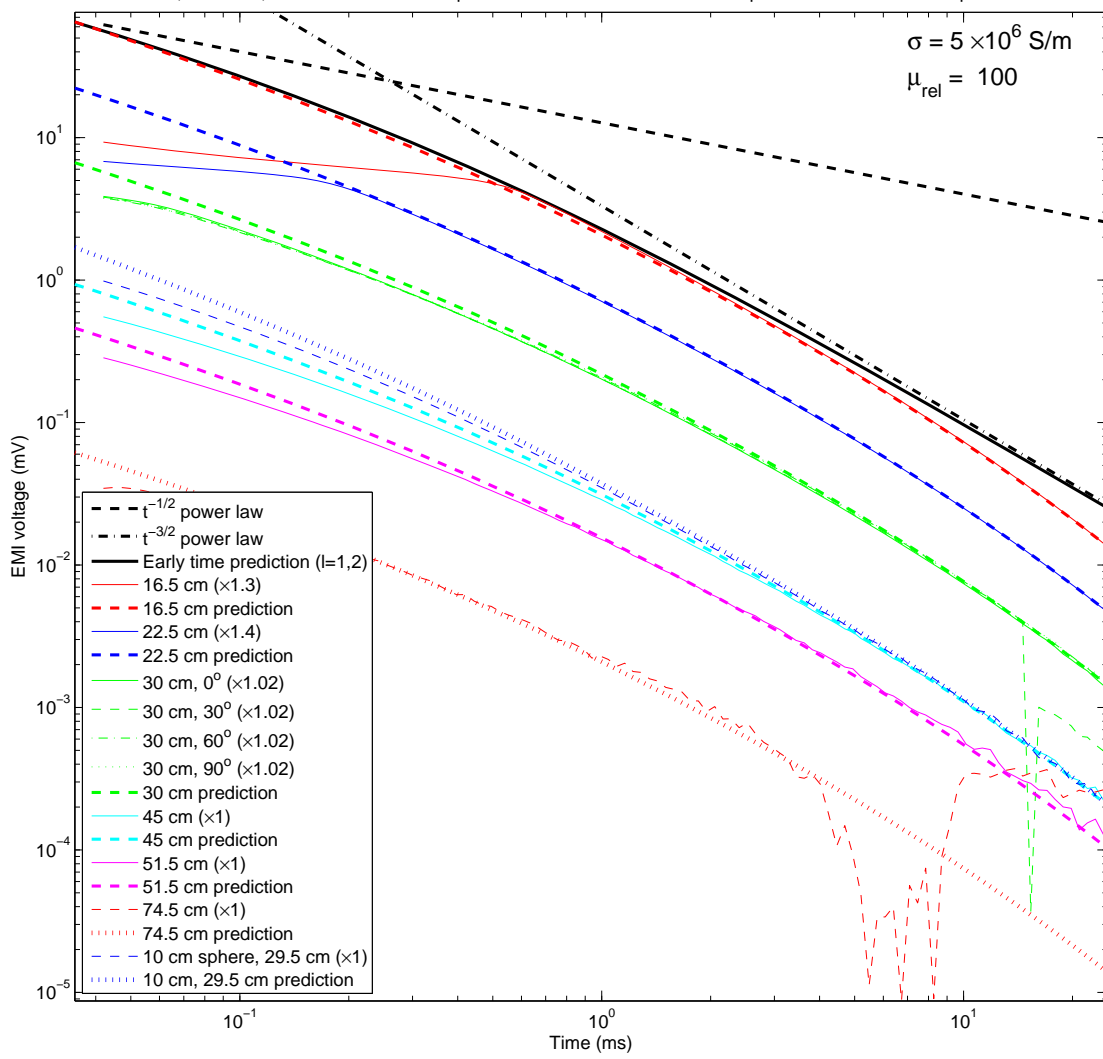
FIG. 10: Consolidated plots showing continuing quantitative agreement between data and theory for the 10 cm and 15 cm diameter steel spheres at various depths centered below sensor 12. The upper curves (16.5 cm depth) are repeated from Fig. 8. The legend shows the multipliers used to scale the data curves for optimal fit. In most cases these lie within the 10% error expected from the variability of the transmitter current. Larger deviations are again likely due to small positioning errors. The four 30 cm depth curves demonstrate the expected invariance of the signal with sphere orientation ("north pole" of the sphere tilted by the indicated angles towards the center of sensor 11). This invariance is not completely obvious for ferrous spheres, since a small remnant magnetization could break the symmetry. The single pair of 10 cm sphere traces demonstrate a much more subtle impact of target size since the data never enter the late-time regime.

tude could equally well come from variation in depth or size of the target. On the other hand, at later time, the traces for smaller targets (e.g., again, the $4 \times 4 \times 20$ cm and $5 \times 5 \times 20$ cm spheroids) drop off much more quickly than those of larger targets.

There are also interesting dependencies on target orientation in this regime (green, red, magenta, and cyan curves for the $10 \times 10 \times 20$ cm spheroid [7]). For a vertical target, the excited modes are dominated by currents the circulate around the symmetry axis, while for a horizontal target the currents tend to circulate along it. The horizontal target mode has a slower decay rate (time con-

stant $\tau_h = 13.7$ ms vs. $\tau_v = 12.0$ ms), and couples differently to the transmitted field, and this is visible in the later-time traces.

Identical conclusions are evident from the data on oblate (discus-like) spheroidal aluminum targets (aspect ratios $\alpha = 0.2, 0.4$) shown in Fig. 12. Here we have overlayed segments of $1/\sqrt{t}$ power law on each curve, explicitly demonstrating successful interpolation (with, perhaps, 5–10% errors in the overlap regime).

The dependence on orientation is much stronger for oblate spheroids (green, red, magenta, and cyan curves for the $20 \times 20 \times 8$ cm spheroid [7]). Because it is be-
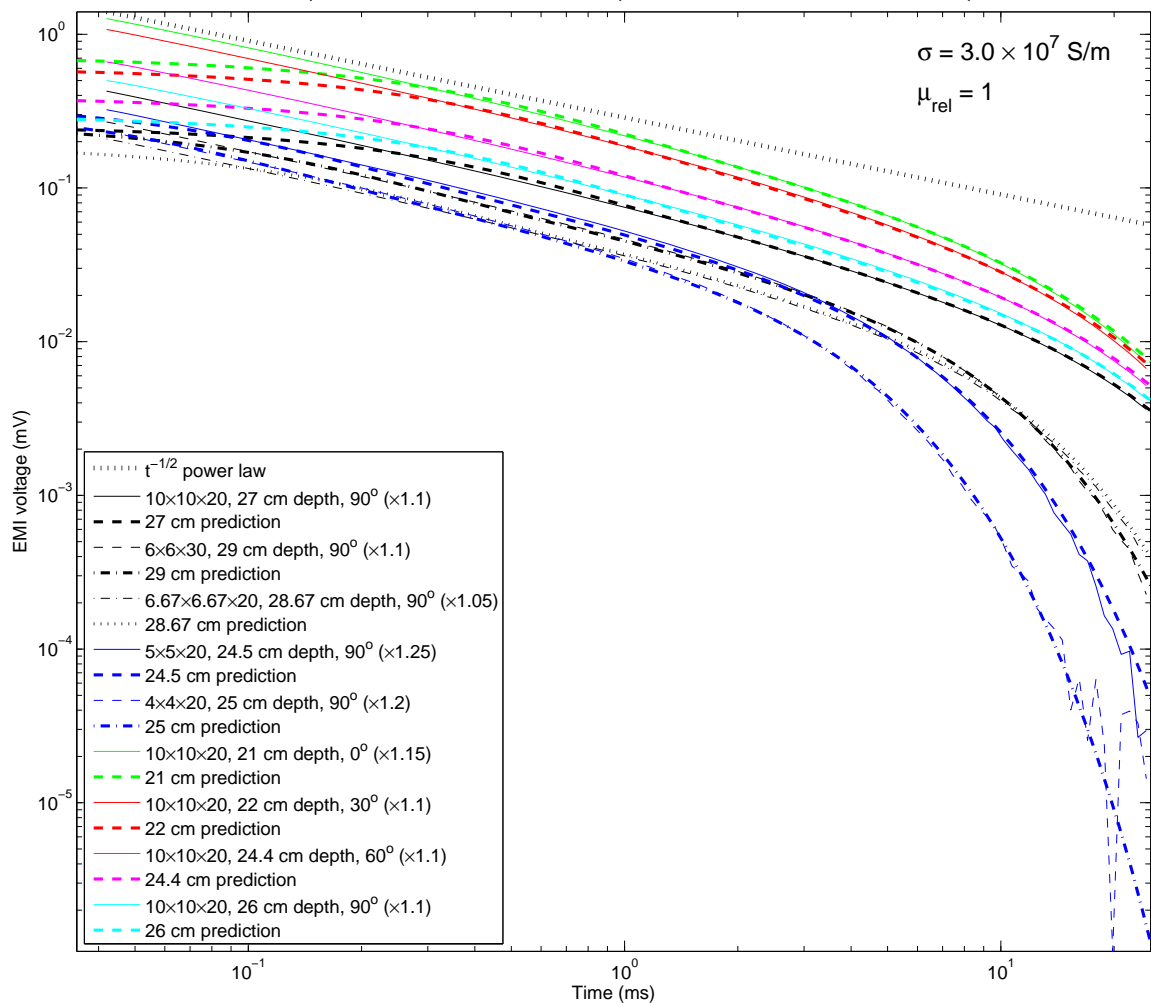
FIG. 11: Consolidated plot of data and theory for a range of artificial aluminum prolate spheroidal targets. The dimensions listed in the legend are diameters. Orientation angles indicate symmetry axis declination (toward the center of sensor 11), so that $0°$ corresponds to vertical and $90°$ to horizontal. The multipliers are again the overall factors applied to the data to obtain optimal agreement with the prediction. The thick dashed lines are the mean field predictions, which show remarkable agreement well into the early time regime, where the onset of the $1/\sqrt{t}$ power law is evident.

ing "squeezed" vertically, the horizontal target (discus on edge) mode now has significantly faster decay rate than vertical target (discus lying flat) mode (time constant $\tau_h = 13.0$ ms vs. $\tau_v = 23.9$ ms). Because the the latter mode is not excited at all when the target is horizontal, the $90°$ (cyan) curve in Fig. 12 dies much more quickly at late time than the other curves.

In both Figs. 11 and 12 the multipliers used to scale the data for optimal fit appear to have a small ($\sim 10\%$) systematic bias that cannot be explained by random variation in the transmitter loop current. A combination of small conductivity and positioning errors is the likely explanation.

Figures 13 and 14 show data and theory for steel prolate and oblate spheroidal targets. As for spherical targets (Figs. 8) and 10), the early time regime dominates, and the mean field results (dotted curves; with S-curve

behavior excised in this case so as not to busy up the plots too much) are valid only over a small part of the time interval where the data is already becoming quite noisy. In most cases, however, the fact that the data is dropping below the early time curve is evident, pointing to the necessity of a multi-exponential description. As before, these predictions actually push quite deeply into the early time regime, but the measurement window, and instrument dynamic range, are such as to strongly limit the information content of the multi-exponential part of the signal.

V. SUMMARY AND CONCLUSIONS

The results presented in this document demonstrate the unprecedented accuracy available from our first prin-
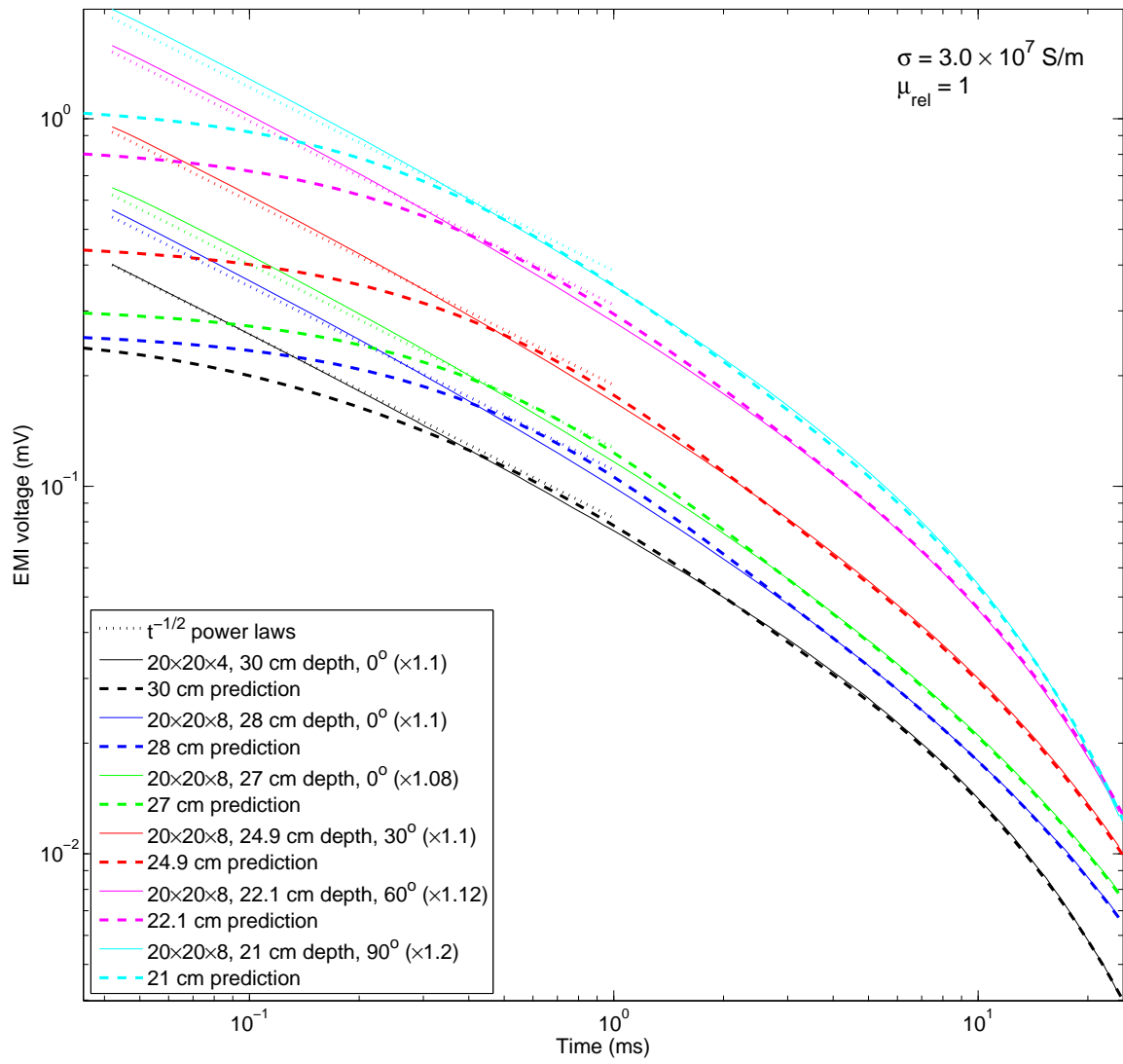
FIG. 12: Consolidated plot of data and theory for a range of artificial aluminum oblate spheroidal targets. The dimensions listed in the legend are diameters. Orientation angles indicate symmetry axis inclination (toward the center of sensor 11), so that $0°$ corresponds to horizontal and $90°$ to vertical. The multipliers are again the overall factors applied to the data to obtain optimal agreement with the prediction. The thick dashed lines are the mean field predictions, which show remarkable agreement well into the early time regime, where the $1/\sqrt{t}$ power law takes over.

ciples, physics based models covering the entire measurement window, from the early time multi-power law regime, all the way through the multi-exponential regime to the late time mono-exponential regime. Prior to the mean field code's current upgrade [8], the number of accurately computed modes used to describe the multi-exponential regime was limited to perhaps a few dozen [9]. As seen in the validation results presented, this upgrade is absolutely critical to the success of the predictions, by generating the required overlap of the early time and multi-exponential regimes.

It should be emphasized that the increase in predictive power continues to operate with extremely high numerical efficiency. The creation of the mode data for a given target cannot be performed in real time, but once this data is made available in a database that spans the expected target geometries, its acquisition and use for measurement predictions can be performed in real time—operating at essentially the same speed as predictions using the exact solution for the sphere.

As seen in the figures, the dominant regimes visible in the data depend very strongly on the target size and physical properties. Increasing target size and magnetic permeability expands the early time regime to later physical time. Smaller aluminum targets (e.g., blue lines in Fig. 11) are completely described by the mean field approach over the full time range, while even the smaller steel targets barely enter multi-exponential regime (see
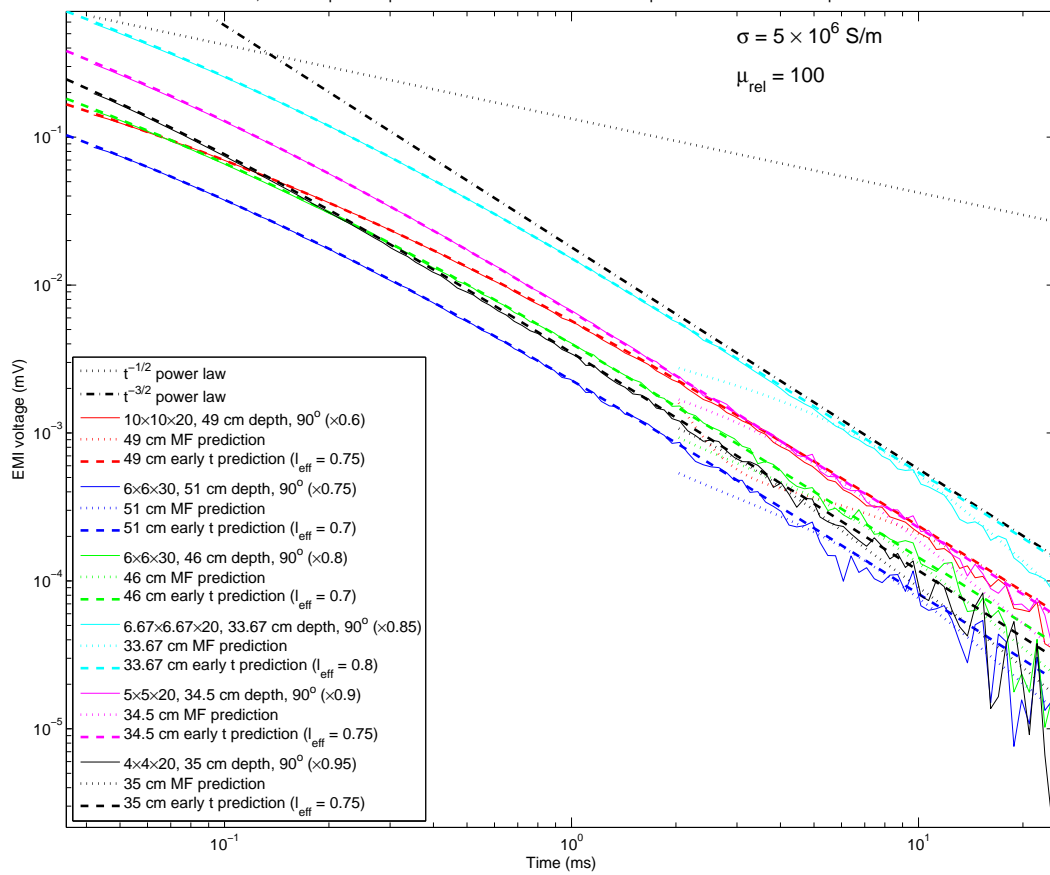
FIG. 13: Consolidated plot of data and theory for a range of steel prolate spheroidal targets. Orientation angles indicate symmetry axis inclination (toward the center of sensor 11), so that $0°$ corresponds to horizontal and $90°$ to vertical. The multipliers are again the overall factors applied to the data to obtain optimal agreement with the prediction. The thick dashed lines are the early time predictions, which show remarkable agreement over nearly the entire measurement window. The latter take the form (2.11) with a *single* term, in which the amplitude V_1^e and eigenvalue $\kappa_1 = l_{eff}/\sqrt{\tau_{mag}}$ are adjusted to optimize the fit. Here τ_{mag} is defined by (2.10) and (2.8), with the choice $L = \min\{a_{xy}, a_z\} = a_{xy}$. The mean field predictions are shown by the dotted lines. If extended over the full time interval, they also would display the S-curve behavior seen in Fig. 8. For these smaller targets, their region of validity begins only as the signal levels are falling into the noise floor. The early time regime therefore pretty much encompasses the full range of useful data.

Figs. 13 and 14) before the signal fades into the noise floor [10].

All of these features, whose quantitative interpretation is enabled by the present models, will be used in pursuit of robust target discrimination and identification in later stages of this project. The code efficiency becomes especially critical for this purpose, as searches through the database for the target whose response best matches the data may require hundreds, or even thousands, of iterations.

[1] P. B. Weichman, *Universal early-time response in high-contrast electromagnetic scattering,* Phys. Rev. Lett. **91**, 143908 (2003).

[2] P. B. Weichman, *Surface modes and multipower-law structure in the early-time electromagnetic response of magnetic targets,* Phys. Rev. Lett. **93**, 023902 (2004).

[3] The external code actually takes the frame of reference issue several steps further. It allows one to specify a horizontal survey grid, with azimuth specified relative to a chosen "north". The height of the platform center (above each grid point) may then be chosen arbitrarily, and the 3D platform orientation about this raised center may also be specified arbitrarily (through specification of three Euler angles). The target 3D position and orientation may then be specified as well.

[4] The divergence eventually saturates even for a perfect, instantaneously terminated, square wave pulse, but only due to speed of light retardation effects in the background medium.

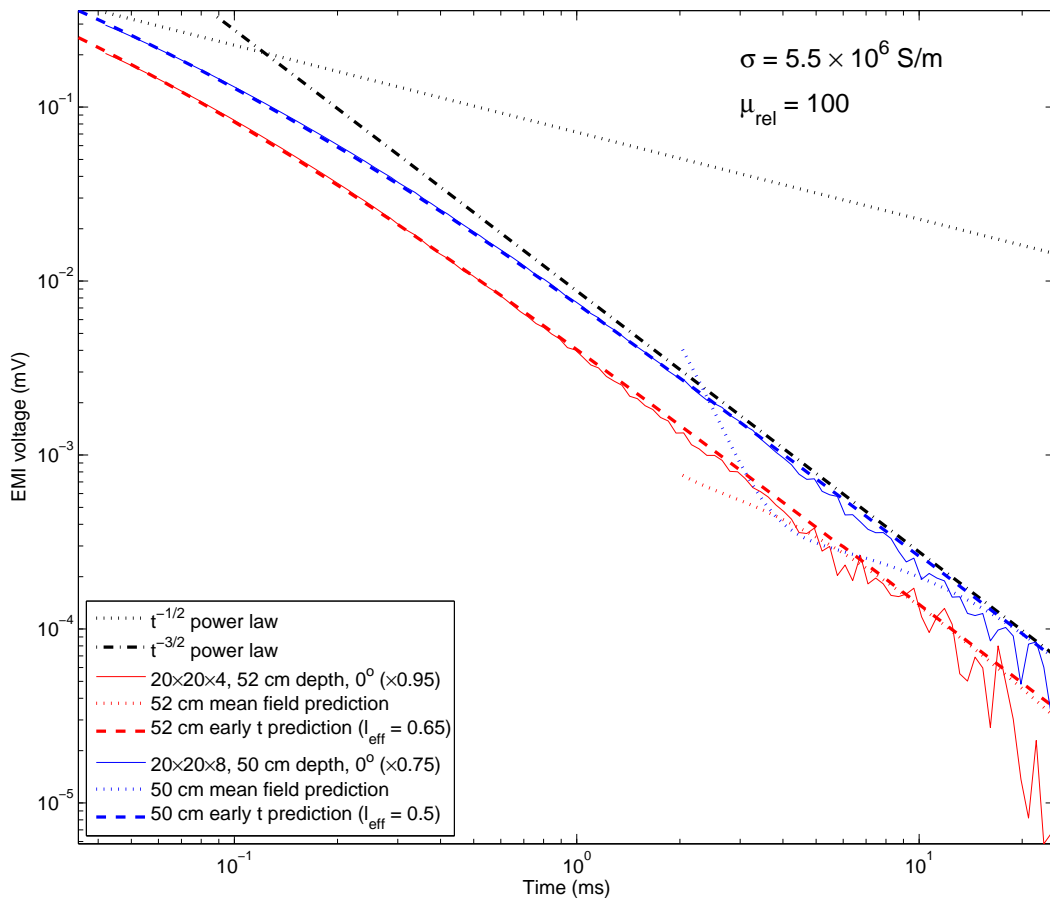[5] See, e.g., J. D. Jackson *Classical Electrodynamics* (John

FIG. 14: Consolidated plot of data and theory for a range of steel oblate spheroidal targets. Orientation angles indicate symmetry axis inclination (toward the center of sensor 11), so that $0°$ corresponds to horizontal and $90°$ to vertical. The multipliers are again the overall factors applied to the data to obtain optimal agreement with the prediction. The thick dashed lines are the early time predictions, which show remarkable agreement over nearly the entire measurement window. The latter take the form (2.11) with a *single* term, in which the amplitude V_1^e and eigenvalue $\kappa_1 = l_{eff}/\sqrt{\tau_{mag}}$ are adjusted to optimize the fit. Here τ_{mag} is defined by (2.10) and (2.8), with the choice $L = \min\{a_{xy}, a_z\} = a_z$. The mean field predictions are shown by the dotted lines. If extended over the full time interval, they also would again display the S-curve behavior seen in Fig. 8. For these smaller targets, their region of validity again begins only as the signal levels are falling into the noise floor, and the early time regime pretty much encompasses the full range of useful data.

Wiley and sons, New York, 1975).

[6] This is far less obvious on the linear-time plot, in which only the $1/t^{3/2}$ late-early time power law is clearly visible. The log-time scale is key to elucidating the multi-scale nature of the target electrodynamics.

[7] For the $10 \times 10 \times 20$ cm and $20 \times 20 \times 8$ cm spheroid measurements, the bottom of the target rested on a platform at 31 cm depth, and so the depth-to-center varies with orientation: between 26 cm (horizontal target) and 21 cm (vertical target) for the former; between 27 cm (vertical target) and 21 cm (horizontal target) for the latter.

[8] A full theoretical description of the algorithm is contained in P. B. Weichman, *Chandrasekhar Theory of Ellipsoidal Scatterers,* BAE Technical Report (2010).

[9] P. B. Weichman and E. M. Lavely, *Study of inverse prob-lems for buried UXO discrimination based on EMI sensor data,* Proc. SPIE Vol. 5089 *Detection Technologies for Mines and Minelike Targets VIII* (SPIE, Bellingham, WA, 2003), p. 1139.

[10] This signal fading is exacerbated by the more rapid $1/t^{3/2}$ decay of the late-early time signal for steel targets, as compared to the much slower $1/t^{1/2}$ aluminum targets. The latter then have greater tendency to maintain strong signals into the multi-exponential regime (see Figs. 11 and 12). As decribed in Sec. II B (see especially Fig. 3), this more rapid decay has its orgin in the surface current dynamics, which, in magnetic targets, tends to more quickly push the currents away from the target surface.